Predicting false alarm rates for high-resolution anti-submarine warfare sonars in a cluttering environment prone to false alarm rate inflation

Karl Thomas Hjelmervik, Henrik Berg, and Tale S Såstad

Manuscript received April XX, 20XX; revised January XX, 20XX. K. T. Hjelmervik, H. Berg, and T. S. Såstad are with the Norwegian Defence Research Establishment (FFI), PO Box 115, 3191 Horten, Norway, e-mail: karl-thomas.hjelmervik@ffi.no

***Abstract*—Operation of high-resolution, broadband anti-submarine warfare (ASW) sonars in littoral waters is challenging, since the presence of sea mounts, underwater ridges and other topographic features causes increased false alarm rates. Two important contributors to the raised false alarm rates are the signal-processing induced phenomenon called false alarm rate inflation (FARI) and the presence of sonar clutter, also referred to as non–Rayleigh distributed matched filter (MF) envelope in literature. Conventional constant false alarm rate (CFAR) algorithms fail to achieve a constant false alarm rate in all ranges and bearing in the presence of such effects.**

Given sufficient information on the bathymetry and the bottom properties, the occurence of FARI may be estimated through the use of an acoustic model. This allows for more accurate estimates of the false alarm rate. Through measurements the scatterer statistics for a given sonar in a given area may be estimated. Combining a FARI predicting scheme with knowledge of the scatterer statistics allows the estimation of the probability of false alarm in the presence of both FARI and sonar clutter.

Here we propose a new detection scheme that employs this approach in order to estimate a range– and bearing–dependent threshold that can be applied on normalized sonar data in order to achieve a constant false alarm rate even in the presence of FARI and clutter. The performance of the method is assessed through the use of receiver operating characteristic curves and is shown to outperform conventional CFAR algorithms, such as the cell averaging (CA), greater of (GO), and ordered statistics (OS) CFAR processors. The method is tested on both recorded and synthetic data. The robustness of the method is tested using synthetic data by introducing errors in the topography, sound speed, and scatterer statistics when estimating the probability of false alarm. The performance of the method decreases when introducing these errors, but it still outperforms the conventional CFAR processors.

I. Introduction

SEA trials in littoral environments have shown that high–resolution active sonars generate particularly many false alarms in presence of terrain features, such as seamounts and underwater ridges, and man-made objects, such as ship wrecks and pipelines [10, 31, 32, 21]. Possible causes for high false alarm rates include false alarm rate inflation (FARI) [33, 21] and non–Rayleigh reverberation [10, 2]. False alarm rate inflation is induced by a non–stationary reverberation power level in the normalizer windows. Non–Rayleigh reverberation, also called clutter, appears when the sonar resolution is so high that the sonar footprint is too small for the central limit theorem to apply to the scatterer statistics [29].

A signal processing chain for a specific sonar system is tuned in order to limit the amounts of false alarms to a manageable level for a human sonar operator. In recent years there has been an increasing interest in using unmanned heterogeneous sensors, for instance autonomous unmanned vehicles (AUV), in anti–submarine warfare (ASW) operations [24, 6, 14]. AUVs rely on acoustic communication links in order to relay their contacts to the decision makers. However, the underwater communication bit rates are far too low to support the transmission of all contacts, particularly in the littorals where high false alarm rates are expected. Other unmanned platforms, such as unmanned surface vehicles or sonobuoys, may be equipped with radio links that allow for streaming of raw data to a human operator, but as the number of sensors per human operator increases, there will be an increased need for signal processing or classification techniques that reduces the number of false alarms further.

In the past decades, a steady rate of research has been published on reducing false alarm rates without reducing the probability of detecting a present target. Improvements in any stage of the signal processing chain that increases the signal–to–noise ratio is a means of reducing the false alarm rate as this allows for a higher detection threshold without reducing the probability of detecting the desired target. However, here we shall focus on the higher level processing steps; normalization, detection, and classification.

Alternative normalization algorithms, also called constant false alarm rate (CFAR) processors, have been proposed to deal with signal processing induced phenomena such as false alarm rate inflation and target masking [33]. The conventional cell averaging (CA) CFAR algorithm is known to exhibit degradation in areas with non–stationary reverberation [37]. Other processors such as the Greatest of (GO) CFAR and the Ordered statistics (OS) CFAR algorithms have been proposed in order to deal with this challenge [15]. More recently, the likelihood ratio test was proposed used for dealing with radar clutter [5], which is the equivalent of non–Rayleigh reverberation.

The problem of false alarms may also be dealt with at other levels of processing. In [3] the authors suggest using a modified version of the Page test for detecting a target. This method exploits information from the entire time spread of the target echo instead of just the strongest peak. Time reversal [25] is another method that deals with the time spreading of

Dette er en postprint-versjon/This is a postprint version.
DOI til publisert versjon/DOI to published version: 10.1109/JOE.2019.2936642

the echo by exploiting accurate knowledge of the environment and an acoustic model in order to focus all energy received from a single target. Clustering techniques have also been used in order to reduce the amount of false alarms by simply collecting threshold crossings in the proximity of each other in a single cluster [7]. Track–before–detect schemes have also shown promise, particularly for targets with low signal–to–noise ratios [11]. These schemes skip the detection step and feed the tracker with sensor data directly.

For an ASW sonar an automatic classifier tries to determine whether a given detection originates from a submarine or not. Techniques involving image processing [35, 13, 27] and feature extraction [16, 32, 30, 7, 38, 17, 18, 20, 22, 36] have been reported in literature. Recently, implementations of deep neural network for automatic image and speech recognition [19, 26] have also inspired work within target classification for active, ASW sonars [8].

Several of these algorithms also employ information on the environment and an acoustic model to either improve detection [25] or classification [21]. Kim et al [25] employed an acoustic model to predict the multipath behaviour of a target echo and then focus this energy into a single sample through a time–reversal technique. This demonstrates how acoustic modelling may be integrated into sonar processing in order to increase the detection performance of a system. Hjelmervik [21] proposed a method for predicting the probability of false alarm due to FARI. An acoustic model and a high-resolution bottom model were employed in order to estimate the probability that a given contact is a false alarm due to FARI. The resulting probability could then be used as a classification feature. However, the proposed method assumes Rayleigh-distributed matched filter output. When using high–resolution sonars in littoral environments the Rayleigh assumption does not always hold [10, 29, 34].

Here we improve and extend the method in [21]. First the method is generalized to include any known non-Rayleigh distribution of the matched filter envelope when estimating the probability of false alarm. Secondly, inspired by how Kim et al [25] incorporates acoustic modelling in the detection process, the method is integrated into the detection step by determining a threshold that achieves a constant false alarm rate even in the presence of FARI and non–Rayleigh reverberation.

The performance of the method is studied using synthetic sonar data in an environment prone to both FARI and non–Rayleigh reverberation. The acoustic raytrace model Lybin [12] is used to estimate both reverberation and target echoes. The performance is compared to conventional methods for dealing with FARI, such as the GO and OS CFAR processors. The comparison is made using receiver operating characteristic (ROC) curves.

Finally, the proposed method is demonstrated on a recorded sonar data set collected in the Norwegian Trench during the New Array Technology 3 (NAT3) programme in 2002. NAT3 was a joint collaboration between TNO, Thales Underwater Systems, the Norwegian Defence Research Establishment, and the Dutch, French, and Norwegian navies.

II. THEORY

The conventional method for determining sonar detections of targets embedded in noise and reverberation is by beamforming, matched filtering, normalizing, and finally thresholding the hydrophone output of the sonar. The processing results in a set of threshold crossings, henceforth called echoes. A few of the echoes may be actual target detections, while most of the echoes are false alarms.

Assuming a Rayleigh–distributed and stationary matched filter envelope, the probability of false alarm, P_{FA}, when using an ideal normalizer depends on the selected threshold in the detection step [33]:

$$P_{FA} \quad = \quad \exp(-h), \tag{1}$$

where h is the applied detection threshold. This follows from the matched filter power being exponentially distributed when the envelope is Rayleigh–distributed. Usually, the detection threshold is selected based on a desired probability of false alarm, thus,

$$h = -\ln P_{FA}. \tag{2}$$

A commonly used normalizing algorithm is the CA CFAR normalizer [33]. The normalizer output, s, is given by:

$$s \quad = \quad \frac{\Lambda}{\mu_\Lambda}, \tag{3}$$

where Λ is the matched filter power output at the analyzed sample. μ_Λ is the background estimate for the analyzed sample, which, for a CA CFAR normalizer is the average power in the normalizer windows, see Fig. 1. For stationary and Rayleigh–distributed matched filter envelopes, the probability of false alarm when using a CA CFAR normalizer approaches that of the perfect normalizer for increasing window sizes [33].

With the above assumptions of Rayleighness and stationarity a sonar may be designed to generate a limited and controlled amount of false alarms. However, in the presence of non–stationary reverberation, (1) does not hold as the background estimate from the normalizer windows may not be representative for the analyzed sample [21]. In Fig. 1 an example of non–stationary reverberation is given. Observe that the peak in the reverberation output at the analyzed sample far exceeds the reverberation levels in the normalizer windows. Even in the absence of a target this reverberation peak results in a threshold crossing with a high estimated signal–to–reverberation and noise ratio, and thus a false alarm. This phenomenon is called false alarm rate inflation (FARI) [33]. A more general expression for the probability of false alarm, that takes into account FARI, is:

$$P_{FA} \quad = \quad \Pr\{s > h\}. \tag{4}$$

The expected reverberation may be modelled using a conventional acoustic model. However, to assess the false alarm rate, the full distribution must also be taken into account. Some high fidelity models are capable of modelling both the expected value of the reverberation power as well as the higher order moments, or even the full distribution [28]. However, here we follow a simpler approach where we let the acoustic

Dette er en postprint-versjon/This is a postprint version.
DOI til publisert versjon/DOI to published version: 10.1109/JOE.2019.2936642

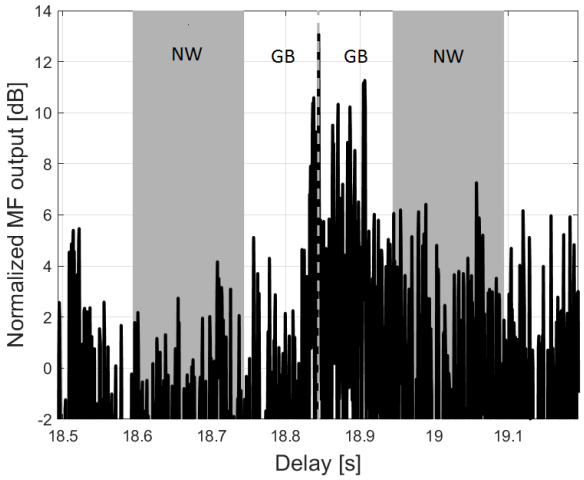

Fig. 1: Illustration of non–stationary reverberation and the location of guard bands (GB) and normalizer windows (NW), as well as the analyzed sample (dashed grey line).

model estimate the expected reverberation power, and then include the desired distribution:

$$\Lambda[i,j] \quad = \quad \lambda[i,j]D[i,j], \tag{5}$$

where $\lambda[i,j]$ is the modelled expected reverberation power for the ith beam and jth time sample. $D[i,j]$ is a random variable. If the matched filter envelope is Rayleigh–distributed, then $D[i,j]$ is exponentially distributed:

$$f_{D[i,j]}\big(D[i,j]\big) \quad = \quad \begin{cases} \exp\big(-D[i,j]\big), & D[i,j] \geq 0 \\ 0, & D[i,j] < 0 \end{cases} \tag{6}$$

Note that, by time, we here mean the delay from transmission untill reception on the receiver. Note that this is directly proportional to range, as the range, r, may be derived from time, t:

$$r \quad = \quad \widehat{c}t, \tag{7}$$

where $\widehat{c}$ is the assumed horizontal speed of sound through the acoustic channel. We assume that the acoustic channel is not frequency selective. For some wide band cases, this may not apply and must then be taken into account in the modelling.

High resolution active sonars have wide bandwidths and narrow beam widths. For some bottom patches only a limited amount of significant scatterers then falls within the sonar footprint, whose area depends on the resolution of the sonar, and therefore its bandwidth and beam width. If the number of scatterers becomes so low that the central limit theorem does not hold, then the matched filter components are no longer Gaussian and it follows that the matched filter envelope is no longer Rayleigh distributed [29]. Here we would like to generalize so that the probability of false alarm may be estimated for any distribution. Inserting (3) and (5) into (4) yields:

$$P_{FA}[i,j] \quad = \quad \Pr\left\{\frac{\lambda[i,j]D[i,j]}{\mu_\Lambda[i,j]} > h\right\}. \tag{8}$$

Literature generally refers to distributions for the matched filter envelope rather than the matched filter power. Bringing (8) down from power level to envelope level and isolating the random variable on the left side give:

$$P_{FA}[i,j] \quad = \quad \Pr\left\{\sqrt{D[i,j]} > \frac{\sqrt{\mu_\Lambda[i,j]h}}{\sqrt{\lambda[i,j]}}\right\}. \tag{9}$$

For a known distribution of $\sqrt{D[i,j]}$, $P_{FA}[i,j]$ may easily be estimated numerically. For some distributions, such as the Rayleigh distribution, the expression may be determined analytically [21]. Since we here generalize the method to apply for any envelope statistics, we estimate this probability numerically. Two different distributions are used; the Rayleigh distribution, $g_R(x)$ and the K–distribution, $g_K(x)$ [28]. The latter distribution has been shown to more accurately model the tail for Non–Rayleigh matched filter envelope data [29, 1, 28]. Other distributions, such as the Weibull and Log–normal distributions, have also been shown to model Non–Rayleigh behaviour well [9], but here we limit the analysis to the Rayleigh and K–distributions. The distributions are given by:

$$g_R(x) \quad = \quad \frac{x}{\sigma^2}\exp\left(\frac{-x^2}{2\sigma^2}\right) \tag{10}$$

$$g_K(x) \quad = \quad \frac{4}{\sqrt{\alpha}\Gamma(\nu)}\left(\frac{x}{\sqrt{\alpha}}\right)^{\nu} K_{\nu-1}\left(\frac{2x}{\sqrt{\alpha}}\right), \tag{11}$$

where x is the normalized matched filter envelope. σ is the scale parameter of the Rayleigh distribution. ν and α are the shape and scale parameters of the K–distribution, respectively. The cumulative density functions (CDF) are given by:

$$G_R(x) \quad = \quad \int_0^x g_R(x')dx' \tag{12}$$

$$G_K(x) \quad = \quad \int_0^x g_K(x')dx'. \tag{13}$$

For a given distribution, threshold, modelled reverberation power, and modelled background estimate the false alarm rate may be estimated [4]:

$$P_{FA}[i,j] \quad = \quad 1 - G(\frac{\sqrt{\mu_\Lambda[i,j]h}}{\sqrt{\lambda[i,j]}}), \tag{14}$$

where G is a CDF, for instance one of the CDFs shown above.

From (14) the threshold, h, to be applied on sample $[i,j]$ in order to achieve a specific false alarm rate may be determined. However, this assumes a perfect spatial synchronization of modelled reverberation and recorded sonar data. Due to the limited sonar aperture and time resolution of the sonar recorded echoes will have an uncertainty in both time and bearing. Errors in the assumed sound speed and sonar position and heading increase the uncertainty further. Also, if the full, range dependent sound speed profile and topography is not fully known, then spatial errors in the estimated reverberation must also be expected.

Let $[\theta,t]$ be the coordinates (bearing, time) relative to the receiver of a false alarm measured on the receiver and let $[\beta[i],\tau[j]]$ be the coordinates of a single modelled sample. If the false alarm in $[\theta,t]$ occurs due to a threshold crossing

Dette er en postprint-versjon/This is a postprint version.
DOI til publisert versjon/DOI to published version: 10.1109/JOE.2019.2936642

event predicted by the model in $[\beta[i], \tau[j]]$, then the bearing and time errors for this realisation is given by:

$$\Delta\theta = \beta[i] - \theta \tag{15}$$

$$\Delta t = \tau[j] - t. \tag{16}$$

The errors are here considered as random variables and approximated as Gaussian distributed with standard deviations of σ_θ and σ_t, respectively. The probability of measuring a false alarm in $[\theta, t]$ due to a threshold crossing event predicted by the model in the model cell with a centre position at $[\beta[i], \tau[j]]$, is given by:

$$F_{ij}(\theta, t) = P_{FA}[i,j] \int_{\theta-\frac{\Delta\Theta}{2}}^{\theta+\frac{\Delta\Theta}{2}} \int_{t-\frac{\Delta T}{2}}^{t+\frac{\Delta T}{2}} f(\theta', t')\, \mathrm{d}t'\, \mathrm{d}\theta', \tag{17}$$

where $f(\theta', t')$ is a two dimensional Gaussian function with standard deviations in θ and t given by the two localization error parameters, σ_θ and σ_t, discussed above. $\Delta\Theta$ and ΔT are the sizes of the model cells for angle and time, respectively. $P_{FA}[i,j]$ applies for the entire model cell and may therefore be considered a constant when integrating over the model cell. The probability of measuring a false alarm in $[\theta, t]$, $\rho_{FA}(\theta, t)$, due to a threshold crossing event predicted in any model cell may then be estimated as follows:

$$\rho_{FA}(\theta, t) = 1 - \prod_{i=1}^{M} \prod_{j=1}^{N} \left(1 - F_{ij}(\theta, t)\right), \tag{18}$$

where M and N are the total amount of modelled samples and beams, respectively.

For a given threshold, h, $\rho_{FA}(\theta, t)$ approximates the false alarm rate in a known environment when using a sonar where the expected errors in time and bearing are given by σ_t and σ_θ. The latter parameters are not easily determined analytically as they depend on a wide variety of uncertainties both connected to the accuracy of the model, the sonar, and the environmental knowledge, but they may be estimated from data. An optimization approach where the quantities are varied untill $\rho_{FA}(\theta, t)$ matches the false alarm rate estimated from recorded data could be carried out. However, this requires accurate modelling of the reverberation peak levels, which requires detailed knowledge of the bottom characteristics, such as sediment density, sound speed, and attenuation. Instead the optimization may maximise the estimated probability of a false alarm in areas with high densities of measured false alarms, and minimize it in areas with low densities of measured false alarms. The optimization employs a genetic search algorithm to estimate both σ_t and σ_θ that maximizes the estimated probability of false alarm for all areas with high densities of measured false alarms following the steps of [22].

In conventional sonar processing, the detection step consists of finding all samples that crosses a set threshold, h. Assuming Rayleigh–distributed matched filter output and an ideal normalizer, then a desired probability of false alarm may be achieved by selecting an appropriate threshold, h, see (2). However, in the Non–Rayleigh case and in areas prone to FARI the achieved false alarm rate may differ strongly from the desired rate. This mismatch may be alleviated by inputting a desired probability of false alarm into (18), and then estimating a time and bearing dependent threshold, $h(\theta, t)$, that satisfies these equations:

$$\rho_{FA} = 1 - \prod_{i=1}^{M} \prod_{j=1}^{N} \left(1 - F_{ij}(\theta, r)\right) \tag{19}$$

$$F_{ij}(\theta, t) = P_{FA}[i,j] \int_{\theta-\frac{\Delta\Theta}{2}}^{\theta+\frac{\Delta\Theta}{2}} \int_{t-\frac{\Delta T}{2}}^{t+\frac{\Delta T}{2}} f(\theta', t')\, \mathrm{d}t'\, \mathrm{d}\theta' \tag{20}$$

$$P_{FA}[i,j] = 1 - G_K\left(\frac{\sqrt{\mu_\Lambda[i,j] h(\theta, t)}}{\sqrt{\lambda[i,j]}}\right). \tag{21}$$

G_K is the CDF for the K-distribution. Note that the distribution parameters are also time and bearing dependent.

A. Sonar data synthesis

In order to assess method performance in a controlled environment, sonar data has been synthesized. The synthetic environment contains nine targets in variable locations and moving along different paths, see Fig. 2. The acoustic model Lybin [12] was employed to estimate both reverberation and target echo strength and structure at matched filter envelope level.

Given (5), the output of the matched filter may be represented by:

$$\sqrt{\Lambda[i,j]} = \sqrt{\lambda[i,j]}\sqrt{D[i,j]}, \tag{22}$$

where $\lambda[i,j]$ is the expected matched filter power and corresponds to the reverberation and noise output of the acoustic model. The reverberation output is upsampled to match the sampling frequency of the sonar. $\sqrt{D[i,j]}$ may be modelled as a random process. Here a K-distribution is used. The target echo is modelled using an eigenray model and the TAP target strength model [23] is used to estimate the echo structure and strength. The resulting echo is added to the synthesized matched filter data at the appropriate samples. Rayleigh distributed noise equivalent to sea state 2 is added to all samples.

B. Normalization and detection

Both the synthetic and the measured matched filter output are run through a normalizer and a detection algorithm. Three different normalizers are used; CA, OS, and GO CFAR normalizers [15]. The normalized output is given by:

$$s[i,j] = \frac{u[i,j]}{n[i,j]}, \tag{23}$$

where $s[i,j]$ is the normalizer output of the j'th time sample in the i'th beam. $u[i,j]$ is the matched filter power level in the corresponding sample. $n[i,j]$ is the estimate of the background level for the same sample. The difference between the three normalizers is how they estimate the background level. CA CFAR estimates the background level as the average of all samples in the normalizer windows, see Fig. 1. GO CFAR estimates the average of each normalizer window separately, and employs the window with the highest average level as the background estimate. Finally, the OS CFAR uses the

Dette er en postprint-versjon/This is a postprint version.
DOI til publisert versjon/DOI to published version: 10.1109/JOE.2019.2936642

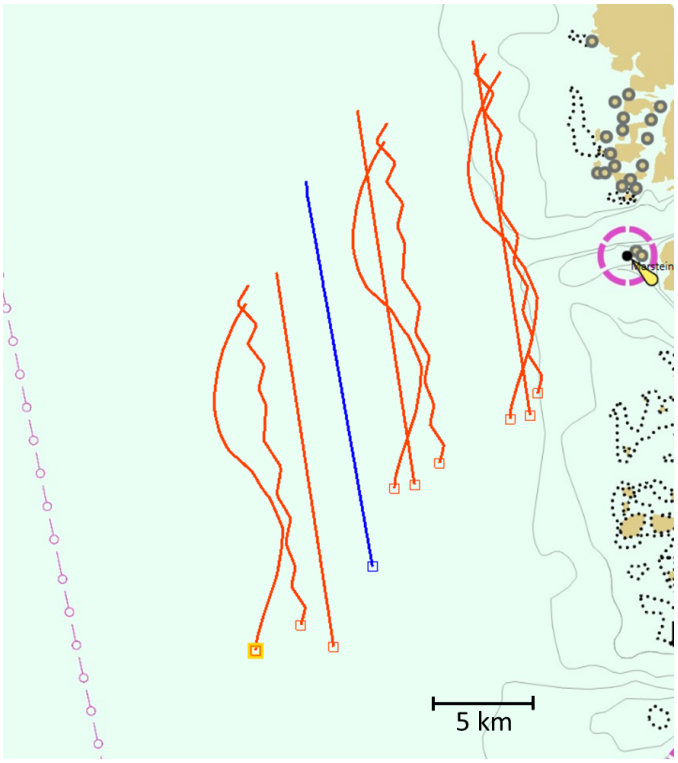

Fig. 2: Path of the research vessel in the Norwegian Trench during the CEX02 experiment is shown in blue. The same path was used in the synthetic data for the sonar vessel. The red paths indicate the movements of the simulated submarines in the synthetic data set. The end point of all paths are indicated by squares. The purple dashed line to the West shows the position of a pipeline that serves as a target of oppurtunity.

median value of the two normalizer windows as its background estimate.

Following normalization a threshold is applied to the data in order to determine the echoes. The threshold is varied in order to estimate receiver operating characteristic (ROC) curves for each approach. Five different schemes are employed as listed in Tab. I. For the GO CFAR and OS CFAR normalizers a conventional threshold constant for all bearings and ranges is used, while for the CA CFAR normalizer both a constant threshold and a bearing– and range–dependent threshold estimated by solving (21) are used. The bearing– and range–dependent threshold is estimated using both a correct distribution for the matched filter envelope (K–distribution with the true parameters) and an erroneous distribution (Rayleigh distribution). (21) is solved for a large number of different ρ_{FA} in order to estimate an ROC curve. In addition to ROC curves, the estimated false alarm rate is plotted against the desired probability of false alarms. For the conventional methods the desired probability of false alarms is given by (1).

III. Results

A. Synthetic data

Data were synthesized in order to compare the performance of the proposed method to conventional methods. The advantage of using synthetic data is that it gives us complete control of the environment and errors in the environment. This allows assessment of how the proposed method responds to different sources of error. Three sources of error are examined:

1) errors in the sound speed profile used in the acoustic model.
2) errors in the topography used in the acoustic model, both due to low quality measurements and lower resolution measurements.
3) errors in the distribution used when determining the threshold in (21). This is covered by the cases where a Rayleigh distribution is used, see FARI in Tab. I.

The synthetic data were generated using a 50 m resolution topographic model and the sound speed profile measured during the CEX02 experiment during the NAT3 trial in 2002. The sound speed profile is shown in Fig. 3. A K–distribution with $\alpha = 0.5$ and $\mu = 1$ was used to model the statistics of the matched filter envelope. Fig. 2 shows the target and sonar vessel positions. Nine targets following different paths and at different depths (60 m, 80 m, and 100 m depth) were simulated. The modelled sonar was placed at 90 m depth and transmitted a two seconds long hyperbolic frequency modulated pulse with a bandwidth of 800 Hz eighty times over two hours. The resulting MF data were processed using all schemes in Tab. I. The normalizer windows were 500 ms wide, while the guard bands were 250 ms wide.

The top part of Fig. 4 shows the ROC curves and the estimated false alarm rate versus the desired probability of false alarm for the error–free environment. The three conventional methods (CA, GO, and OS) using a constant threshold all result in a false alarm rate several magnitudes higher than what is desired. When using a bearing– and range–dependent threshold, but not taking into account the Non–Rayleigh behaviour of the reverberation (FARI), the observed false alarm rate improves by almost a magnitude. Assuming perfect knowledge of both the environment and the Non–Rayleigh behaviour of the reverberation (FARI NR), the desired false alarm rate is achieved. The detection performance of each method may be compared through the use of ROC curves, see Fig. 4. The methods that employ a variable threshold clearly outperform the three conventional methods for false alarm rates below 10^{-3}.

In order to assess the robustness of the method for an erroneous sound speed profile, the modelling used to estimate the bearing– and range–dependent threshold was estimated using a different sound speed profile, see Fig. 3. Both sound speed profiles were measured in September in the same region (Norwegian Trench) and are therefore similarly shaped. This simulates the case where a sound speed profile measured at a different location is used in the acoustic modelling necessary to employ the proposed method. The resulting ROC curves and false alarm rates are shown in Fig. 4. For an estimated false alarm rate of 10^{-5}, the estimated detection rate falls from approximately 50% to approximately 40% when applying the variable threshold. The remaining three methods remain unchanged as expected, but are included as a reference. When using a variable threshold and taking into account the Non–Rayleigh behaviour the desired false alarm rate is still

Dette er en postprint-versjon/This is a postprint version.
DOI til publisert versjon/DOI to published version: 10.1109/JOE.2019.2936642

Tag	Normalizer	Threshold	MF envelope
CA	Cell averaging	Constant for all bearings and ranges	Not relevant
GO	Greater of	Constant for all bearings and ranges	Not relevant
OS	Ordered statistics	Constant for all bearings and ranges	Not relevant
FARI	Cell averaging	Bearing– and range–dependent threshold	Rayleigh
FARI NR	Cell averaging	Bearing– and range–dependent threshold	Non–Rayleigh

TABLE I: Overview of detection schemes employed.

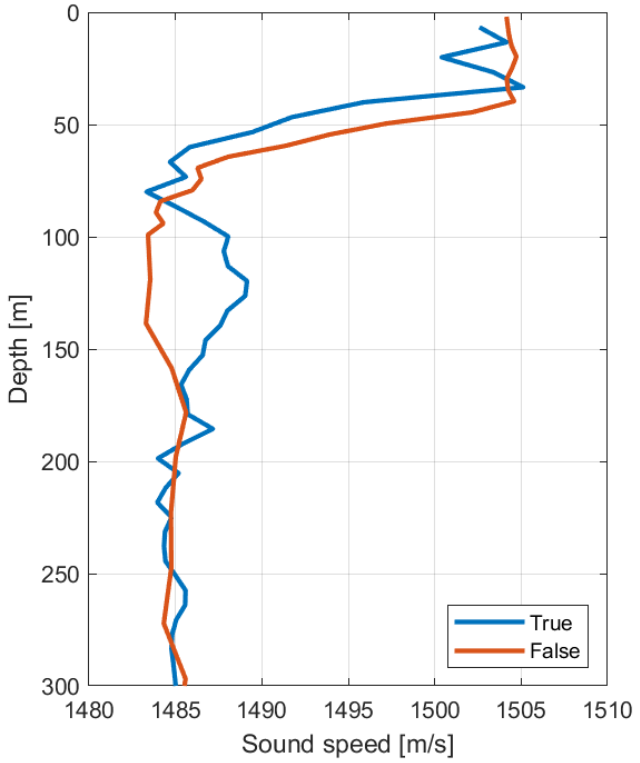

Fig. 3: The sound speed measured during the CEX02 experiment (true) was used when synthesizing the data. The second sound speed profile (false) was used in the modelling to estimate ρ_{FA} when determining the bearing– and range–dependent threshold for the case with the erroneous sound speed profile.

achieved, even though the detection performance is slightly degraded.

When applying zero–mean Gaussian noise with a standard deviation of 5 m to the topography used in the modelling when estimating the threshold, the detection performance falls from 50% to approximately 40%. This simulates the case were low quality topographic data is used in the acoustic modelling necessary to employ the proposed method. The observed degradation is similar to the degradation observed for an erroneous sound speed profile. If Non–Rayleighness is handled, then the desired false alarm rate is still achieved. Similarly, the case where only a low resolution topography data set is available is simulated by degrading the resolution of the topographic model from 50 m resolution to 250 m resolution. The degradation in the results are similar to what was observed for the low quality topographic data.

B. Recorded data

The NAT3 program carried out a large number of experiments on active, low-frequency towed array sonar systems in sea trials in 2001 and 2002. One of the experiments, the Clutter Experiment 2 (CEX02), was carried out in the Norwegian Trench in September 2002. The sea was calm during the experiment. The experiment was designed to assess the performance of low frequency towed arrays close to the coast line.

FFIs research vessel, H U Sverdrup II, towed both a receiver array and a source. The receiver array consisted of equally spaced triplet hydrophones. A towed body, the TNO Socrates source, transmitted a two seconds long hyperbolic frequency modulated pulse with 800 Hz bandwidth every 90 s. The received hydrophone time series were processed up to echo level, using a conventional line array and cardioid beamformer, and matched filter, before using all five normalization and detection approaches described in Tab. I. A guard band of 250 ms and a normalizer window of 500 ms were used, see Fig. 1.

Fig. 2 shows the path of HU Sverdrup II. Easterly bearings (towards the shore) are characterized by an, on average, upsloping and rocky bottom with the occasional presence of sea mounts. Such an environment typically results in highly variable and strong reverberation levels [21]. Westerly directions, on the other hand, are characterized by a fairly constant and flat bottom (approximately 300 m deep), resulting in low and slowly varying reverberation levels and therefore fewer false alarms. The sound speed profile measured at the start of the experiment is shown in Fig. 3.

The upper part of Fig. 5 shows measured matched filtered data after normalization (CA CFAR), along with the corresponding bottom profiles for two different processed beams. The strong peaks observed in the beam pointing towards the shore originate from bathymetric features such as seamounts and ridges close to the coast. Such peaks typically result in both false alarm rate inflation and target masking [33]. Due to the calm weather during the experiment, the measured reverberation is assumed to be mainly due to bottom interaction.

The normalized matched filter data may be used to estimate the scale and shape parameters for both the K–distribution and the Rayleigh distribution. Fig. 6 shows the measured normalized matched filter envelope distributions for a one second interval, 15 seconds into each of the two beams in Fig. 5. The measurements in each interval are fitted with both the Rayleigh and K-distribution following an exhaustive search scheme using a maximum likelihood estimator following the

Dette er en postprint-versjon/This is a postprint version.
DOI til publisert versjon/DOI to published version: 10.1109/JOE.2019.2936642

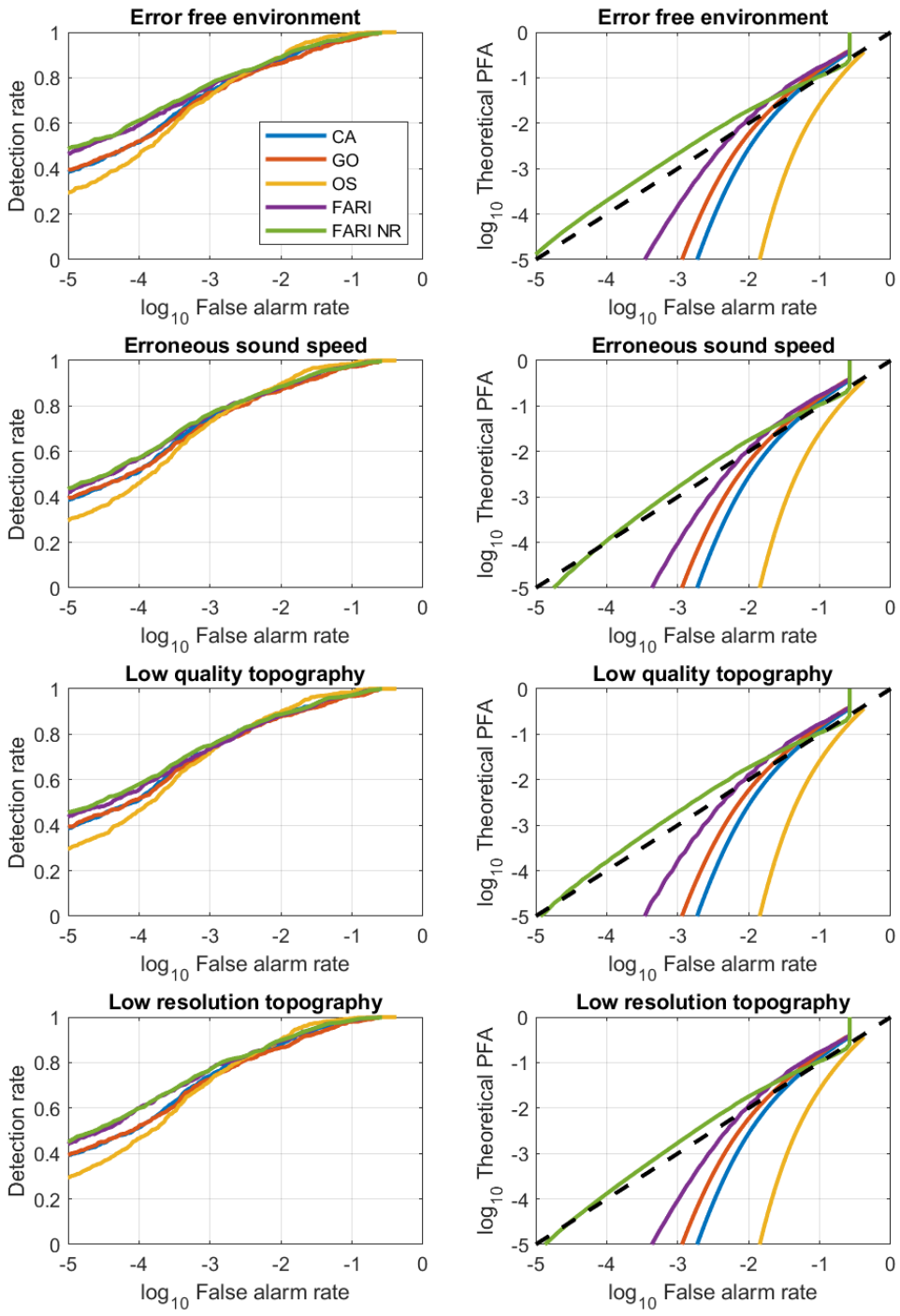

Fig. 4: Left: ROC curves based on synthetic data for all targets and all transmissions. Right: Comparison of measured false alarm rate to the desired probability of false alarm. The results comprise all four scenarios, from top to bottom: No errors, error in water column sound speed, error in the bottom depths, and low resolution bottom.

Dette er en postprint-versjon/This is a postprint version.
DOI til publisert versjon/DOI to published version: 10.1109/JOE.2019.2936642

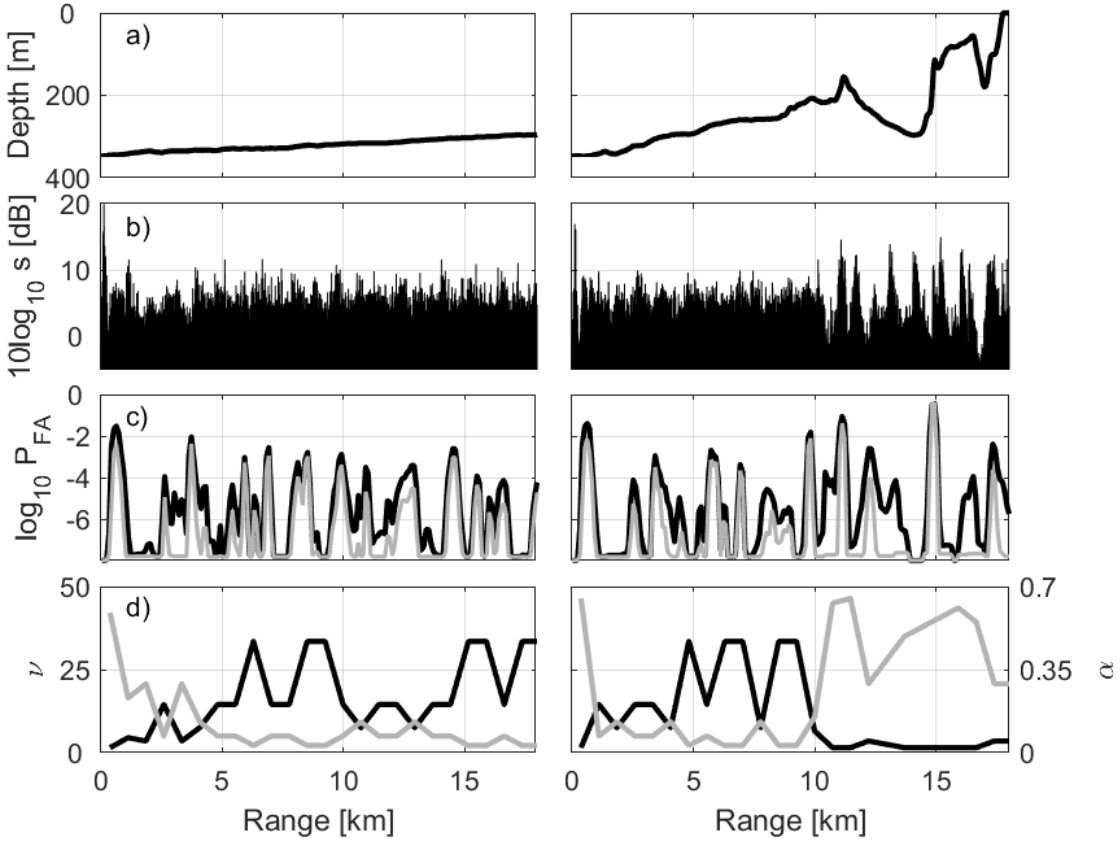

Fig. 5: Left: Beam pointing towards the West. Right: Beam pointing towards the East. a): Bottom profile along the beam. b): Normalized matched filter output using a CA CFAR normalizer with a normalizer window of 500 ms and guard band of 250 ms. c): Probability of false alarm before smoothing, P_{FA}, see (14), along the beam both when applying a Rayleigh distribution (grey) and a K–distribution (black). d): The estimated shape, ν (black), and scale, α (grey), parameters along the beam for the K–distribution.

steps of [34]. Note that such measurements should be made in the absence of any strong targets to skew the measurements. Thus, for real operations, the parameters of the distribution used should be estimated from controlled, historical trials, rather than data during the actual operation. Observe the Rayleigh–like behaviour of the measured data in the beam pointing away from the coast (West) and the strong non–Rayleigh behaviour of the one pointing towards the coast (East). The heavy–tailed distribution of the measurements towards the shore is indicative of a high false alarm rate and the tail is also well–represented by the K–distribution.

The fitting of the distribution parameters is made for each one second interval in all beams. The resulting distributions are then used to describe the random variable $D[i,j]$ in (9). Fig. 5 shows the predicted probability of false alarm, P_{FA}, for the above–mentioned two beams using both the Rayleigh distribution and the K–distribution when modelling the envelope statistics. The selected threshold, h (4), is here given by $10\log_{10} h = 12$ dB. In absence of FARI and assuming Rayleigh distributed matched filter envelope, then, according to [33], the false alarm rate should be slightly higher than 10^{-7}. For the Rayleigh–case, due to both target masking and FARI, the false alarm rate differs from the theoretical value. The K–distributed case often results in even higher false alarm rates than observed for the Rayleigh–case due to the heavier tailed distribution.

The estimated shape and scale parameters for the K–distribution are shown in Fig. 5. For high shape parameters, $\nu >> 0$, the K–distribution is approximately equal to the Rayleigh distribution, as is the case for the distributions shown in Fig. 6 for the beam pointing to the West. Thus, for high values of ν the estimated probability of false alarm using the K–distribution and the Rayleigh distribution are approximately the same. For instance, observe in Fig. 5 that for the first 10 km ν is high and P_{FA} is approximately the same when using both distributions. An exception is at 8 km East due to a local decrease in ν. On the other hand, the predicted probability of false alarm is significantly higher when the shape parameter is low. Observe also that areas with low shape parameters coincide well with areas with reverberation peaks, that is areas already prone to raised false alarm rates due to FARI. This underlines the importance of taking into account both the occurence of FARI as well as the statistics of the matched filter envelope when estimating the probability of false alarm. For this environment, either one alone underestimates the false alarm rate. Note that the presence of reverberation peaks may also bias the estimate of the parameters for the K–distribution. Ideally, a larger and independent sonar data

Dette er en postprint-versjon/This is a postprint version.
DOI til publisert versjon/DOI to published version: 10.1109/JOE.2019.2936642

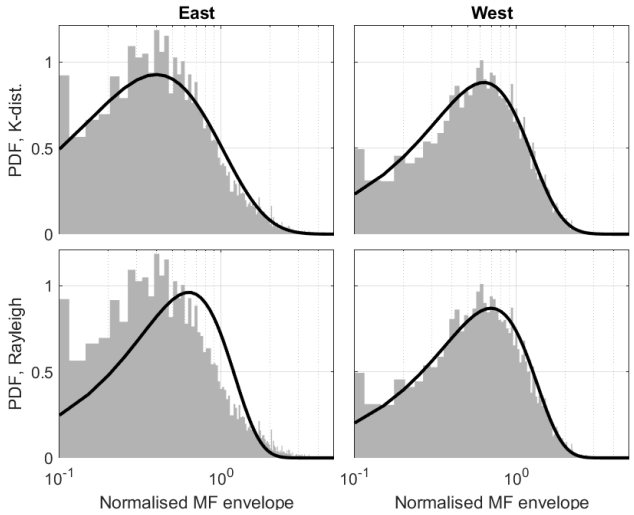

Fig. 6: Normalized matched filter envelope data for beams pointing East (left) and West (right) in a one second wide window 15 seconds (11 km) after transmission. The envelope data are plotted together with the Rayleigh (bottom) and K–distribution (top) fitted to the envelope data.

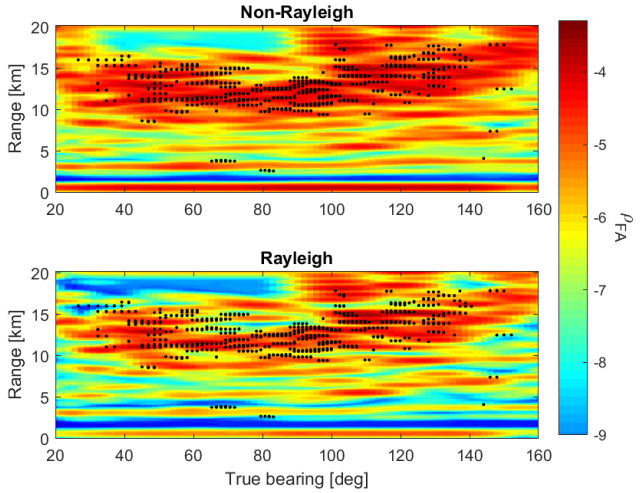

Fig. 7: Estimated probability of false alarm after taking into account the localisation errors (18) as a function of bearing and range for both the Rayleigh–case (bottom) and K–distributed case (top) for the first transmission. Echoes using CA CFAR normalization with a constant threshold of 12 dB for this particular transmission are included as well (black dots). Note that only beams pointing towards the coast are included.

set measured using the same or an equivalent sonar should have been used to map the parameters of the K–distribution. By accumulating data from many different runs, scattering statistics for smaller bottom patches may be estimated. The resulting high resolution map would be less prone to biases due to non–stationary reverberation since each resolution cell would apply for a smaller area.

Figure 7 shows the predicted probability of false alarm plotted in polar coordinates, $\rho_{FA}(\theta, r)$ for a single transmission of the sonar using both the Rayleigh distributed and K–distributed statistics. $\rho_{FA}(\theta, r)$ is generally higher when using the K–distributed statistics, and particularly in areas with high densities of measured echoes.

Figure 8 shows echoes as a function of bearing and range for a single transmission for three different detection schemes; CA, FARI, and FARI NR, see Tab. I. Observe that the estimated bearing– and range–dependent threshold is high for bearings close to 80° and ranges beyond 10 km. At these bearings and ranges the terrain is strongly upsloping and the soft upper sediments becomes thinner for increasing ranges and gives away to naked rock where the ascent is steepest. An example of such a bottom profile is given in Fig. 5 a) right column. When using CA CFAR and a constant threshold a large number of false alarms are generated in this region. These echoes are the main cause for the failure of conventional methods to achieve the desired false alarm rate. The proposed methods, FARI and FARI NR, both exhibit far lower false alarm rates in this region and therefore achieve false alarm rates significantly closer to the desired probability of false alarm. FARI NR outperforms FARI in terms of false alarm rate by taking into account the Non–Rayleigh characteristics of the steep upslopes and rocky terrain in this region.

To the West of the sonar vessel a pipeline is frequently detected using all detection schemes, see Fig. 2 for the location of the pipeline. Fig. 9 shows the ROC curve for all five methods listed in Tab. I. The target is located in a flat region where the threshold estimated by the proposed methods is approximately the same as the one used by the conventional methods, see Fig. 8. The performance of the different schemes in detecting this target is approximately equal, but the total number of false alarms generated vary strongly. Surprisingly, the FARI NR method has slightly lower detection performance than FARI. This is attributed to a contamination of the estimates of the parameters for the K–distribution at the target location. The source of the contamination is the target itself as its echoes influence the tail of the resolution and thereby makes the distribution less Rayleigh. It is a subtle difference, but sufficient to result in an observed performance difference between the two methods. This underlines the importance of using a separate and independent data set free of targets in order to estimate the scattering statistics. Unfortunately, for this analysis no such data set is available, but through extended operation of a sonar system in an area sufficient statistics may be accumulated over time to generate accurate maps of the scattering statistics.

IV. Conclusion

A method for predicting the false alarm rate both in the presence of non-Rayleigh reverberation and reverberation peaks generating false alarm rate inflation has been demonstrated. The method employs an acoustic model fed with highly detailed bottom profiles in order to estimate reverberation. For a given threshold in the detection scheme used, a range– and bearing–dependent probability of false alarm may then be estimated using any known distribution to describe the matched filter envelope statistics. The proposed method may then be used to estimate a bearing– and range dependent

Dette er en postprint-versjon/This is a postprint version.
DOI til publisert versjon/DOI to published version: 10.1109/JOE.2019.2936642

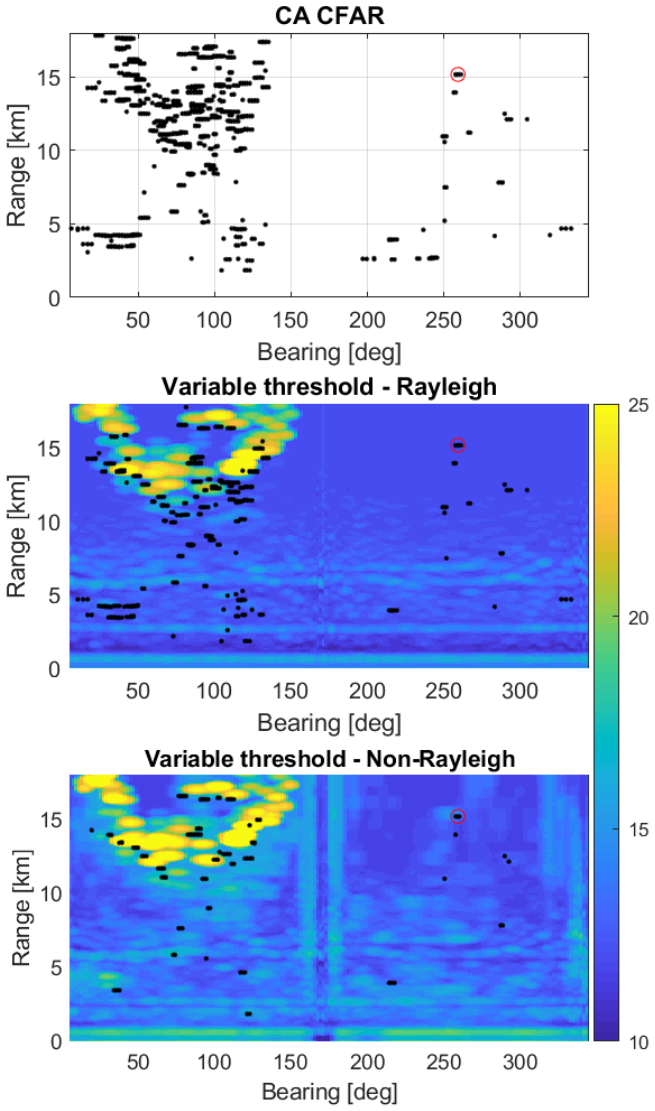

Fig. 8: Top: Processed echoes for a single transmission using CA CFAR normalization and a constant threshold of 12 dB. Bottom and center: The bearing– and range–dependent thresholds estimated by the proposed method for both the Rayleigh case (center) and the Non–Rayleigh case (bottom) overlayed with the resulting echoes. In both cases a bearing– and range–dependent threshold corresponding to a desired false alarm rate of $10^{-5.5}$ is used. The red circle shows the location of a detected pipeline to the West of the sonar vessel. See Fig. 2 for the location of the pipeline.

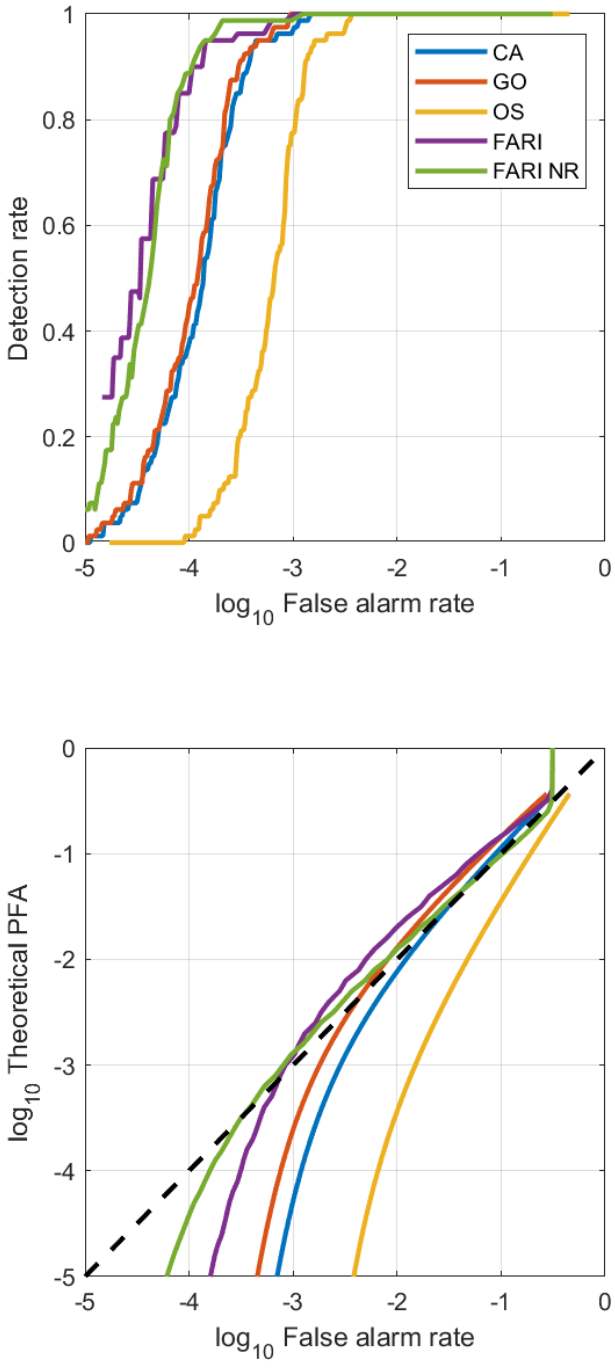

Fig. 9: Top: ROC curves for all methods in Tab. I based on all transmissions in the recorded data set for a pipeline target. Bottom: Comparison of measured false alarm rate and desired probability of false alarm for all five methods using the recorded data set.

Dette er en postprint-versjon/This is a postprint version.
DOI til publisert versjon/DOI to published version: 10.1109/JOE.2019.2936642

threshold that results in a bearing– and range–independent probability of false alarm.

The method was first applied on a synthetic data set. The synthetic data set was generated using an acoustic model input with high–resolution topographic data, a realistic sound speed profile, and by using non–Rayleigh scattering characteristics. Target echoes were also synthesized by using an eigenray approach combined with a simple target strength model.

Five different detection schemes were employed. Three conventional normalizers (CA CFAR, OS CFAR, and GO CFAR) were combined with a constant threshold and compared to two schemes combining a CA CFAR normalizer with a range– and bearing–dependent threshold. The first of the two schemes employed a Rayleigh distributed matched filter envelope, while the second employed a K–distribution (non–Rayleigh distribution). The latter matched the distribution used to generate the synthetic data. The schemes using the variable threshold outperformed the conventional schemes in terms of false alarm reduction. The robustness of the proposed method was tested by introducing realistic errors in both the sound speed profile and the topography used in the acoustic modelling necessary to obtain the range– and bearing–dependent threshold. Even with the induced errors the proposed schemes outperformed the conventional methods, although with reduced performance compared to the error–free environment. The best performance was observed when correctly accounting for the Non–Rayleighness.

The five detection schemes were also applied on a recorded data set collected in the Norwegian Trench. For the scheme that accounts for the non–Rayleigh matched filter envelope, the parameters of the K–distribution were determined directly from the data set by exhaustive search using a maximum likelihood estimator. For operative use of the proposed method the parameters of the K–distribution should be priorly known through historic measurements. The schemes employing range– and bearing–dependent thresholds outperform the conventional schemes also when applied on recorded data.

ACKNOWLEDGMENT

The authors would like to thank the partners of the NAT3 project for making the sonar data from the sea trial available for this publication. We would also like to thank the editor and reviewers for valuable advice and comments that led to a significant improvement of the manuscript.

REFERENCES

[1] Douglas A Abraham and Anthony P Lyons. “Novel physical interpretations of K-distributed reverberation”. In: *Oceanic Engineering, IEEE Journal of* 27.4 (2002), pp. 800–813.

[2] Douglas A Abraham and Anthony P Lyons. “Reverberation envelope statistics and their dependence on sonar bandwidth and scattering patch size”. In: *Oceanic Engineering, IEEE Journal of* 29.1 (2004), pp. 126–137.

[3] Douglas A Abraham and Peter K Willett. “Active sonar detection in shallow water using the Page test”. In: *Oceanic Engineering, IEEE Journal of* 27.1 (2002), pp. 35–46.

[4] Robert Bares, Dafydd Evans, and Stephen Long. “Noise estimation in long-range matched-filter envelope sonar data”. In: *IEEE Journal of Oceanic Engineering* 35.2 (2010), pp. 230–235.

[5] Thomas J Barnard and Fyzodeen Khan. “Statistical normalization of spherically invariant non-Gaussian clutter”. In: *Oceanic Engineering, IEEE Journal of* 29.2 (2004), pp. 303–309.

[6] Robert Been et al. “Cooperative anti-submarine warfare at NURC moving towards a net-centric capability”. In: *OCEANS 2010 IEEE-Sydney*. IEEE. 2010, pp. 1–10.

[7] SP Beerens and W Boek. “A robust algorithm for LFAS target classification”. In: *Undersea Defence Technology-UDT Europe* (2007).

[8] Henrik Berg and Karl Thomas Hjelmervik. “Classification of anti-submarine warfare sonar targets using a deep neural network”. In: *OCEANS 2018 MTS/IEEE Charleston*. IEEE. 2018, pp. 1–5.

[9] Erik P Blasch and Mike Hensel. *Fusion of distributions for radar clutter modeling*. Tech. rep. AIR FORCE RESEARCH LAB WRIGHT-PATTERSON AFB OH, 2004.

[10] NP Chotiros et al. “Acoustic backscattering at low grazing angles from the ocean bottom. Part II. Statistical characteristics of bottom backscatter at a shallow water site”. In: *The Journal of the Acoustical Society of America* 77.3 (1985), pp. 975–982.

[11] Samuel J Davey, Mark G Rutten, and Brian Cheung. “A comparison of detection performance for several track-before-detect algorithms”. In: *EURASIP Journal on Advances in Signal Processing* 2008 (2008), p. 41.

[12] E Dombestein and K E Wegger. *Lybin 6.2 - User manual*. Tech. rep. 2014/00512. FFI, 2014.

[13] S Dugelay and D A Abraham. *Reduction of low frequency active sonar clutter through image processing*. Tech. rep. SR-272-UU. SACLANTCEN, 1999.

[14] Gabriele Ferri et al. “A non-myopic, receding horizon control strategy for an AUV to track an underwater target in a bistatic sonar scenario”. In: *Decision and Control (CDC), 2014 IEEE 53rd Annual Conference on*. IEEE. 2014, pp. 5352–5358.

[15] Prashant P Gandhi and Saleem A Kassam. “Analysis of CFAR processors in homogeneous background”. In: *Aerospace and Electronic Systems, IEEE Transactions on* 24.4 (1988), pp. 427–445.

[16] R Paul Gorman and Terrence J Sejnowski. “Analysis of hidden units in a layered network trained to classify sonar targets”. In: *Neural networks* 1.1 (1988), pp. 75–89.

[17] Doug Grimmett and Cherry Wakayama. “Specsweb post-tracking classification method”. In: *Information Fusion (FUSION), 2011 Proceedings of the 14th International Conference on*. IEEE. 2011, pp. 1–8.

[18] Doug Grimmett, Cherry Wakayama, and Randall Plate. “Multistatic post-track classification using a target strength function”. In: *Information Fusion (FUSION), 2012 15th International Conference on*. IEEE. 2012, pp. 2339–2346.

[19] G E Hinton et al. “Deep Neural Networks for Acoustic Modeling in Speech Recognition: The Shared Views of Four Research Groups”. In: *IEEE Signal Processing Magazine* 29.6 (Nov. 2012), pp. 82–97. ISSN: 1053-5888. DOI: 10.1109/MSP.2012.2205597.

[20] Karl Thomas Hjelmervik. “Automatic classification for mid-frequency anti-submarine warfare sonars - recognizing pipelines”. In: *Presented at the UAC Conference*. 2014.

[21] Karl Thomas Hjelmervik. “Predicting sonar false alarm rate inflation using acoustic modeling and a high-resolution terrain model”. In: *Oceanic Engineering, IEEE Journal of* 35.2 (2010), pp. 278–287.

[22] Karl Thomas Hjelmervik et al. “Optimised prediction of false alarm rate inflation for anti-submarine warfare sonars employed in littoral waters”. In: *Presented at the UDT Conference*. 2016.

[23] Richard P Hodges. *Underwater acoustics: Analysis, design and performance of sonar*. John Wiley & Sons, 2011.

[24] David T Hughes et al. “Sensible behaviour strategies for AUVs in ASW scenarios”. In: *OCEANS 2010 IEEE-Sydney*. IEEE. 2010, pp. 1–7.

[25] S Kim et al. “Echo-to-reverberation enhancement using a time reversal mirror”. In: *The Journal of the Acoustical Society of America* 115.4 (2004), pp. 1525–1531.

[26] A Krizhevsky, I Sutskever, and G E Hinton. “Imagenet classification with deep convolutional neural networks”. In: *Advances in neural information processing systems* (2012).

[27] R Laterveer. *Single ping clutter reduction - segmentation using Markov random fields*. Tech. rep. SR-307. SACLANTCEN, 1999.

[28] Kevin D. LePage. “Statistics of Broad-Band Bottom Reverberation Predictions in Shallow-Water Waveguides”. In: *Oceanic Engineering, IEEE Journal of* 29.2 (2004), pp. 330–346.

[29] Anthony P Lyons and Douglas A Abraham. “Statistical characterization of high-frequency shallow-water seafloor backscatter”. In: *The Journal of the Acoustical Society of America* 106.3 (1999), pp. 1307–1315.

[30] Scott Philips, James Pitton, and L Atlas. “Perceptual feature identification for active sonar echoes”. In: *OCEANS 2006*. IEEE. 2006, pp. 1–6.

[31] Mark K Prior. “A scatterer map for the Malta Plateau”. In: *Oceanic Engineering, IEEE Journal of* 30.4 (2005), pp. 676–690.

[32] Mark K Prior and Alberto Baldacci. “The physical causes of clutter and its suppression via sub-band processing”. In: *OCEANS 2006*. IEEE. 2006, pp. 1–6.

[33] Mark A Richards. *Fundamentals of radar signal processing*. Tata McGraw-Hill Education, 2005.

[34] Tale S Såstad and Karl Thomas Hjelmervik. “Synthesizing realistic, high-resolution anti-submarine sonar data”. In: *OCEANS 2018 IEEE-Kobe*. IEEE. 2018.

[35] Frances B Shin, David H Kil, and Richard F Wayland. “Active impulsive echo discrimination in shallow water by mapping target physics-derived features to classifiers”. In: *Oceanic Engineering, IEEE Journal of* 22.1 (1997), pp. 66–80.

[36] Dan Henrik Sekse Stender et al. “Assessing the performance of kinematic track features for classification of sonar targets in anti-submarine warfare”. In: *Presented at the UDT Conference*. 2016.

[37] M Weiss. “Analysis of some modified cell-averaging CFAR processors in multiple-target situations”. In: *IEEE Transactions on Aerospace and Electronic Systems* 1 (1982), pp. 102–114.

[38] Victor W Young and Paul C Hines. “Perception-based automatic classification of impulsive-source active sonar echoes”. In: *The Journal of the Acoustical Society of America* 122.3 (2007), pp. 1502–1517.